nature
structural &
molecular biology

Cryo-electron tomography reveals that dynactin recruits a team of dyneins for processive motility

Danielle A. Grotjahn[1], Saikat Chowdhury [1], Yiru Xu[1], Richard J. McKenney[2], Trina A. Schroer[3] and Gabriel C. Lander [1]*

Cytoplasmic dynein is a protein complex that transports molecular cargo along microtubules (MTs), playing a key role in the intracellular trafficking network. Vertebrate dynein's movement becomes strikingly enhanced upon interacting with dynactin and a cargo adaptor such as BicaudalD2. However, the mechanisms responsible for increased transport activity are not well understood, largely owing to limited structural information. We used cryo-electron tomography (cryo-ET) to visualize the 3D structure of the MT-bound dynein–dynactin complex from *Mus musculus* and show that the dynactin–cargo adaptor complex binds two dimeric dyneins. This configuration imposes spatial and conformational constraints on both dynein dimers, positioning the four motor domains in proximity to one another and oriented toward the MT minus end. We propose that grouping multiple dyneins onto a single dynactin scaffold promotes collective force production, increased processivity, and unidirectional movement, suggesting mechanistic parallels to axonemal dynein. These findings provide structural insights into a previously unknown mechanism for dynein regulation.

P recise spatial and temporal delivery of components to specific locations within a cell requires tightly regulated trafficking across a vast MT network[1]. A key player in intracellular trafficking is cytoplasmic dynein-1 (hereafter dynein), which transports molecular cargo toward MT minus ends. Dynein functions as a multisubunit complex of dimerized 'heavy chains' (DHCs), containing a C-terminal 'motor' domain (MD) and an N-terminal 'tail' region that contains a dimerization domain and attachment sites for several noncatalytic subunits. The dynein motor is distinct from other cytoskeletal motors, composed of an AAA+ ATPase ring interrupted by a coiled-coil stalk with a globular microtubule-binding domain (MTBD)[2,3]. Notably, purified vertebrate dynein exhibits limited, diffusive movement on MTs. Long-range, minus-end-directed movement requires the association of dynactin, a megadalton-sized multisubunit cofactor, as well as one of various cargo adaptors, such as the N-terminal fragment of BicaudalD2 (BICD2N)[4,5]. Mutations that disrupt these dynein–cofactor interactions are associated with a variety of neurological pathologies[6]. Although the manner by which BICD2N structurally mediates interactions between the dynein tail and dynactin has been elucidated by cryo-EM[7], a fundamental question remains: How do interactions with the dynein tail confer unidirectional processivity on the dynein MDs?
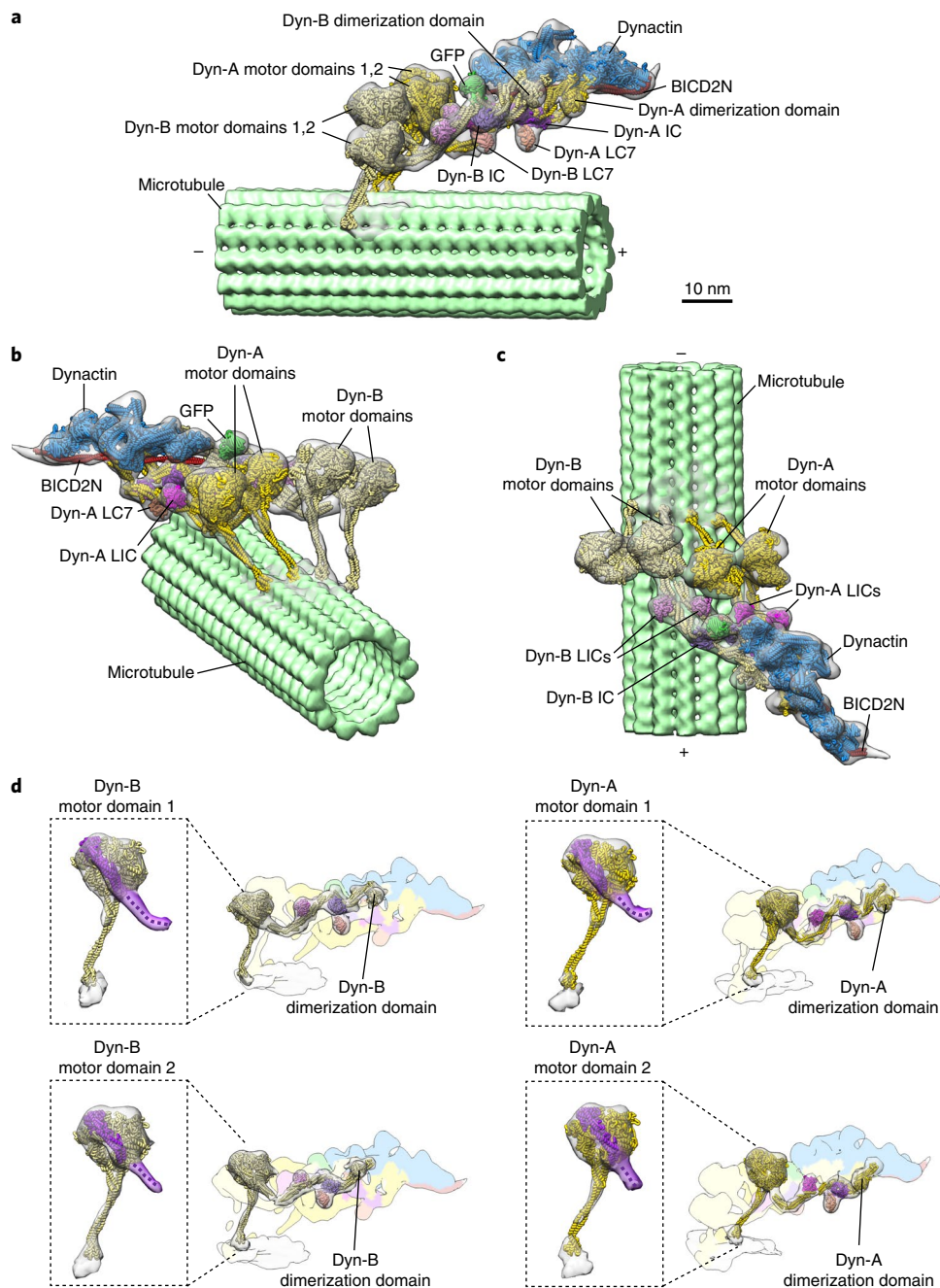
Results

Structure of MT-bound dynein–dynactin–BICD2 complex. To understand how dynein is harnessed to yield processive movement, we isolated dynein–dynactin–BICD2N (DDB) complexes bound to microtubules (DDB–MT) from mouse brain tissue, following methods previously described[8]. The sparse, nonperiodic decoration of DDB complexes bound to MTs, as well as the thickness of the ice required to completely embed intact complexes in all orientations around the MTs, precluded the application of traditional single-particle cryo-EM methodologies. Thus, we used cryo-ET

and subtomogram averaging to determine the 3D structure of this massive, extremely flexible, and asymmetric complex (Fig. 1, Supplementary Figs. 1 and 2 and Supplementary Video 1).

To facilitate the 3D reconstruction of this complex, we developed and integrated an assisted alignment procedure into the RELION subtomogram averaging workflow[9], then performed focused refinement of the individual components (dynein tails–dynactin–BICD2N (TDB) and each pair of dynein motors) (Supplementary Figs. 3 and 4 and Methods). The resulting structures were merged in UCSF Chimera[10] to obtain the final reconstruction of the intact DDB–MT complex (Fig. 1, Supplementary Fig. 5 and Methods).

BICD2N mediates the association of two dynein dimers with a single dynactin. The overall organization of the DDB–MT complex resembles those of previous structures[7,8], but a striking new feature emerged: the presence of two complete dimeric dynein densities bound to dynactin (Fig. 1). The details of the reconstruction were sufficient to visualize the entirety of the four DHCs from the dynactin-bound N terminus to the C-terminal MDs and to confirm the post-power-stroke conformation of the motor linker domain[11,12], which is consistent with the presence of AMP-PNP during the isolation procedure (Fig. 1d). The four MDs are positioned in a row, ~17 nm from the MT surface, with weak density attributable to the stalk contacting the corresponding MT. Additionally, the structure displays densities for several other dynein subunits, including the light intermediate chain (LIC), light chain 7 (LC7), and intermediate chain (IC) (Fig. 1), in positions that are consistent with previous studies[2,7,8]. The majority of the dynein subunits were rigid-body docked into the DDB–MT structure using individual chains from previous atomic models of human cytoplasmic dynein-1 complexes (EMD-5NW4, PDB 5NVS), although short segments proximal to the MDs had to be repositioned to fit the cryo-EM density. The resulting model of the complete DDB–MT complex shows the organization of two dynein dimers (Dyn-A and Dyn-B) with associated

[1]Department of Integrative Structural and Computational Biology, The Scripps Research Institute, La Jolla, CA, USA. [2]Department of Molecular and Cellular Biology, University of California-Davis, Davis, CA, USA. [3]Department of Biology, Johns Hopkins University, Baltimore, MD, USA. Danielle A. Grotjahn and Saikat Chowdhury contributed equally to this work. *e-mail: glander@scripps.edu
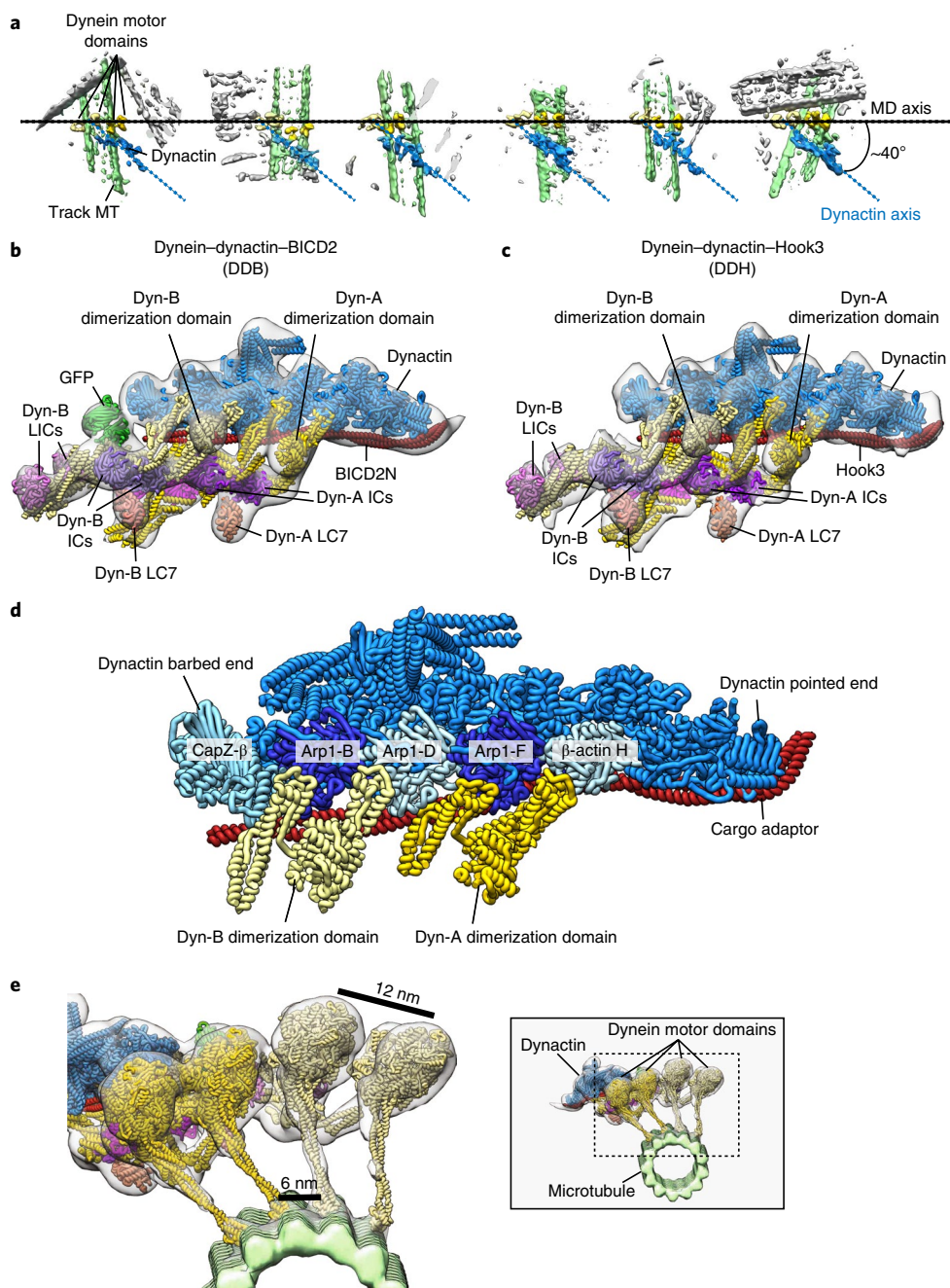
Fig. 1 | 3D organization of the MT-bound dynein–dynactin–BICD2N complex. a–c, Three views of the subtomogram average (gray transparent density) of the MT–DDB complex are shown, with fitted atomic models of dynein dimer-1 (Dyn-A, yellow), dynein dimer-2 (Dyn-B, light yellow), dynactin (blue), BICD2N (red), associated chains (purple, salmon, and magenta), and the BICD2N GFP tag (green) and a microtubule model (light green). PDB IDs used in fitting are listed in Methods. **d,** Cryo-EM density for each dynein HC and associated subunits with docked models, with the remainder of the cryo-EM density colored according to component composition (color scheme same as that described for **a–c**). Boxed regions focus on the cryo-EM density of each motor domain, showing the linker arm (purple) in the post-power-stroke conformation, consistent with AMP-PNP binding.

dynein subunits, one dynactin–BICD2N complex, and the GFP-tag at the N terminus of BICD2N (Fig. 1a).

The observation that the dynactin–BICD2N assembly binds to two dynein dimers in the presence of MTs is unexpected, because prior motility assays and structural studies concluded that only one dynein dimer was present in the dynactin–BICD2N complex[2,4,5,7] (Fig. 1 and Supplementary Fig. 6a,d). Manual inspection of the individual raw subtomograms revealed that over 97% of the dynactin densities were associated with four dynein MDs (Fig. 2a and Supplementary Fig. 2b). Importantly, 3D refinement
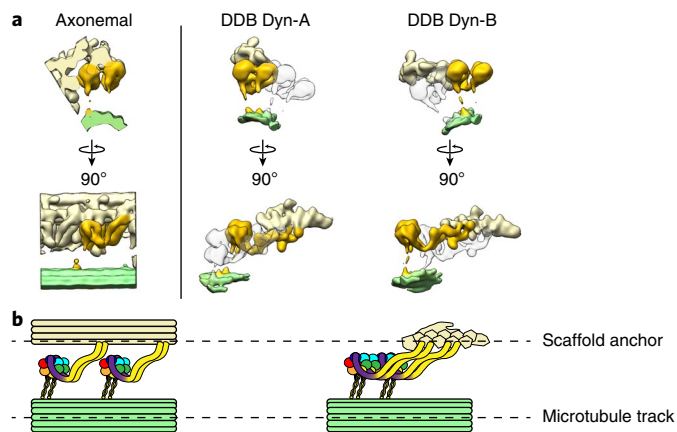
improved the quality of the dynactin density and also revealed poorly resolved density corresponding to four MDs (Supplementary Fig. 6b). Focused 3D classification on the region surrounding the dynein MDs did not yield any well-resolved 3D classes containing a single dynein dimer (Supplementary Fig. 6c), thus reinforcing our conclusion. Furthermore, comparison of our reconstruction with previously determined 2D averages of negatively stained DDB–MT complexes[8] revealed highly correlated structural features (Supplementary Fig. 6d), suggesting that two dynein dimers were associated with a single dynactin in our

Fig. 2 | Association of two dyneins with dynactin in the presence of cargo adaptor proteins. a, Raw subtomograms show that dynein dimers (MDs in light yellow and yellow) associate with a single dynactin (blue) in Dyn–adaptor–MT complexes. The MDs are arranged horizontally (axis represented by black dotted line), showing that the dynactin is oriented at a ~40° relative to the MD to the axis. The DDB-associated MT is in green; nonassociated MTs are in gray. **b,c**, Subtomogram averages (gray transparent density) of the dynactin–dynein tail–cargo adaptor portion of the DDB–MT (**b**) and DDH–MT (**c**) complexes with docked atomic models of dynein tails (color scheme same as in Fig. 1). Both complexes present a similar overall architecture with two dimeric dyneins bound to a single dynactin. **d**, A pseudoatomic model of the dynactin–dynein tail–cargo adaptor complex shows interactions between two dimeric dynein tails and the dynactin filament. The tail of Dyn-A binds to dynactin across the Arp1-F subunit, with one heavy chain binding at the interface between β-actin H and Arp1-F and the other at the interface between Arp1-F and Arp1-D. The tail of Dyn-B binds across the Arp1-B subunit of dynactin, with one heavy chain binding at the interface between the Arp1-B and Arp1-D subunits and the other between Arp1-B and CapZ-β. **e**, Subtomogram average (gray transparent density) of the DDB–MT complex with fitted atomic models (as shown in Fig. 1) shows that spacing between ATPase rings and MTBDs is ~12 nm and ~6 nm, respectively. The position of the MDs relative to the entire DDB–MT complex is shown in the inset (right).

earlier 2D averages of the DDB–MT complex[8]. Prior 2D analyses probably hindered the visualization of the four dynein MDs, owing to flattening effects of the methodology compounded by the inability to discern overlapping motor densities from a projection image.

The ability of BICD2N to facilitate binding of two dynein dimers to a single dynactin complex may explain why a subset of DDB complexes exhibited extreme run lengths (>50 μm) in motility assays[5]. Furthermore, recent single-molecule experiments show that DDB complex velocities on MTs distribute into two populations,

Fig. 3 | Organizational and mechanistic commonalities between axonemal dynein and cytoplasmic dynein, suggesting a model for processivity.
a, Left, orthogonal views of the axonemal dynein subtomogram average (EMD-5757, ref. [21]). Axonemal dynein (gold) associates with an MT doublet scaffold (light yellow) through its tail and another MT doublet (green) through the MT-binding stalk of the motor. Right, the organization of cytoplasmic dyneins in dynein–dynactin–cargo adaptor–MT complexes. Each of the two dimeric dyneins (Dyn-A and Dyn-B) are in gold and associate with the dynactin scaffold (light yellow) via the tails and to the MT surface (light green) through the MT-binding stalk of the motors.
b, Similarities between the overall organization of multiple axonemal dyneins in the axoneme (left) and two cytoplasmic dyneins in Dyn–cargo adaptor–MT complexes (right) are shown using diagrammatic representations. Each AAA+ domain with the dynein motor domain is in a different color, with the linker arm colored purple. In both systems, multiple dyneins are associated with a filamentous scaffold (MT doublet or dynactin) via N-terminal tail interactions. The dynein motors associate with MT tracks through the binding stalk. In this way, both axonemal and cytoplasmic dyneins integrate into scaffolds to work in teams.

with one exhibiting twice the velocity of the other[13]. Additionally, recent structural studies have shown that dynactin–BICD2N is capable of binding two dimeric dyneins in the absence of MTs[14]. Together, these data suggest that regulatory mechanisms exist that influence the DDB's dynein/dynactin stoichiometry and that perhaps inclusion of AMP-PNP in our brain lysate, which immobilizes DDB complexes on MTs for structural analyses, may have induced a dynein conformation that favors the observed 2:1 stoichiometry.

Hook3 also recruits two dynein dimers to dynactin. To assess whether the recruitment of two dynein dimers is unique to the BICD2N scaffold, we isolated dynein–dynactin complexes bound to MTs in the presence of another cargo adaptor, an N-terminal fragment of Hook3, which was also shown to endow dynein–dynactin with processive motility[5,15,16]. Strikingly, the subtomogram average of the resulting dynein–dynactin–Hook3 (DDH) complex again revealed two tail domains interacting with dynactin and EM density attributable to two sets of dynein's accessory subunits (LC, IC, LIC) (Fig. 2c and Supplementary Fig. 7). The fact that the structures of DDH and DDB are largely indistinguishable (Fig. 2b,c and Supplementary Fig. 7) suggests that recruitment of two dynein molecules to the dynactin–cargo adaptor complex is a widely conserved mechanism for inducing processive motility.

Our 3D reconstructions illustrate how one dynactin–adaptor complex can accommodate two dynein dimers. The previously determined TDB structure showed the dynein tail to be bound to two clefts along dynactin's Arp filament: one between Arp1-D and Arp1-F and the other between Arp1-F and β-actin H (ref. [7]). We observed identical interactions here (Fig. 2b,c). The second dynein

tail binds the Arp1 filament in a highly similar fashion, interacting with two adjacent clefts near the barbed end of dynactin, one between Arp1-D and Arp1-B and the other between Arp1-B and the CapZ-β dimer (Fig. 2b–d). The fact that neither our study nor previous studies observe complexes in which dynein straddles the clefts in the center of the Arp filament (i.e., on either side of Arp1-D) suggests that the dynactin–cargo adaptor interface has evolved to maximize dynein occupancy on dynactin.

Motor domains are positioned for processive motility. In contrast to previous structural studies of isolated DDB complexes[7,8,14], our structure reveals the spatial organization of the dynein MDs relative to the dynactin complex. Formation of the stable TDB complex appears to constrain the dynein motors in a semiparallel organization on the microtubule (Figs. 1 and 2a). The MDs are visible but poorly resolved in the cryo-EM reconstruction before focused refinement of these domains (Supplementary Fig. 6b), suggesting that the TDB architecture constrains the lateral positioning of the motors around the MT, yet allows sufficient flexibility to facilitate the conformational changes necessary for dynein motility. Focused refinement of the MDs shows that they are equidistantly spaced ~12 nm apart, with all four MTBDs projecting toward the MT minus end (Figs. 1b,c and 2e). Interestingly, there is some variability in the transverse angle at which the MD pairs attach to the MT axis, which limits our ability to resolve individual tubulin dimers on the MT lattice (Figs. 1 and 2a). Regardless, the spacing between the MTBDs is consistent with the MT helical protofilament spacing, suggesting that the four MDs associate with four distinct but adjacent MT protofilaments (Fig. 2e). Notably, interactions of the dynein tail with dynactin's helical Arp filament yield a conspicuous 'skewed' organization in which dynactin is oriented approximately 40° relative to the linear array of dynein motors (Fig. 2a).

To confirm that the dynein MD configuration on MTs is promoted by the dynactin–adaptor complex, we used cryo-ET to visualize dynein dimers bound to MTs in the absence of dynactin and adaptors. Manual inspection of 229 subvolumes showed that isolated dynein dimers bind the MT surface individually, with their MDs at a range of distances from one another (Supplementary Fig. 8), thus hindering our ability to generate a 3D average of these complexes. Despite this complication, our results suggest that in the absence of cofactors, individual cytoplasmic dynein complexes bind individually to the MT, with the two MDs positioned at variable distances from one another. Thus, not only does the dynactin–cargo adaptor complex recruit multiple dyneins, it positions their MDs in an array that is highly compatible with unidirectional processive movement. This finding is consistent with prior work showing that association of a single dynein with dynactin results in a dramatic reorganization of dynein from an autoinhibited conformation to one that is capable of productive minus-end movement[2].

Discussion
In addition to positioning the dynein MDs for processive motility, dynactin can also serve as a scaffold for collective force production. Vertebrate dynein motors have been shown to work collectively to generate forces that far exceed those produced by an individual dynein motor[17,18], and this multimotor coordination may be required to carry out high-load transport processes, such as nuclear positioning, mitotic-spindle rotation, and organelle trafficking. A well-characterized example of teamwork among dynein motors can be found in ciliary and flagellar axonemes, where axonemal dyneins are known to work in huge ensembles to accomplish large-scale synchronized ciliary and flagellar motility[19].

We wondered whether the dynein configuration observed in our structures showed any similarities to that of axonemal dynein. Axonemal dyneins contain a C-terminal MD that is

similar to that of cytoplasmic dynein, but have evolved a distinct N-terminal tail to accommodate its cellular function[20]. Intriguingly, the spatial organization and 3D shape of not only the dynein MDs, but also much of the tail domain in the DDB–MT structure is strikingly similar to that of sea urchin sperm flagella outer dynein arms in the post-power-stroke state[21] (Fig. 3a and Supplementary Fig. 9). In both structures, dynein tails exhibit a flexible 'kink' domain projecting from the linker arm, which extends away from the MD to associate with an elongated, filamentous structure—a microtubule doublet in the case of axonemal dynein and dynactin's actin-like filament in the case of cytoplasmic dynein (Fig. 3b). This leads us to hypothesize that cytoplasmic and axonemal dyneins utilize a similar mechanism for coordinating the activity of multiple dynein motors, in which parallel arrangement of the MDs relative to the MT allows the conformational change associated with ATP hydrolysis to propel the MTBD more effectively toward the MT minus end[21]. Another non-mutually exclusive possibility is that the second motor might increase the duty ratio of the entire complex by providing an additional attachment to the MT lattice and reducing the probability of complex dissociation from the MT during movement. Such an effect could enhance complex processivity, as has been observed in assays that multimerize motors on an artificial scaffolding, such as a bead or DNA chassis[22–24]. Given that a range of duty ratios are observed in different types of axonemal dyneins[25], further study will be required to investigate the extent of the structural parallels between axonemal and cytoplasmic dynein and if there exist additional regulatory commonalities or evolutionary divergences. However, because of the technical challenges in structurally characterizing this large, conformationally heterogeneous complex, investigating these proposed mechanisms of dynein motility will require a combination of more sophisticated reconstitution systems and improved cryo-ET methodologies.

In conclusion, the MT–dynactin–dynein-adaptor complexes presented here provide a platform that integrates decades of biochemical and biophysical studies on the unusual behavior of this large, highly conserved, minus-end-directed motor protein while posing further interesting questions regarding the underlying mechanisms of dynein-mediated intracellular transport.

Methods

Methods, including statements of data availability and any associated accession codes and references, are available at https://doi.org/10.1038/s41594-018-0027-7.

References

1. Welte, M. A. Bidirectional transport along microtubules. *Curr. Biol.* **14**, R525–R537 (2004).
2. Zhang, K. et al. Cryo-EM reveals how human cytoplasmic dynein is auto-inhibited and activated. *Cell* **169**, 1303–1314.e18 (2017).
3. Schmidt, H. & Carter, A. P. Review: Structure and mechanism of the dynein motor ATPase. *Biopolymers* **105**, 557–567 (2016).
4. Schlager, M. A., Hoang, H. T., Urnavicius, L., Bullock, S. L. & Carter, A. P. In vitro reconstitution of a highly processive recombinant human dynein complex. *EMBO J.* **33**, 1855–1868 (2014).
5. McKenney, R. J., Huynh, W., Tanenbaum, M. E., Bhabha, G. & Vale, R. D. Activation of cytoplasmic dynein motility by dynactin-cargo adapter complexes. *Science* **345**, 337–341 (2014).
6. Hoang, H. T., Schlager, M. A., Carter, A. P. & Bullock, S. L. DYNC1H1 mutations associated with neurological diseases compromise processivity of dynein-dynactin-cargo adaptor complexes. *Proc. Natl. Acad. Sci. USA* **114**, E1597–E1606 (2017).
7. Urnavicius, L. et al. The structure of the dynactin complex and its interaction with dynein. *Science* **347**, 1441–1446 (2015).
8. Chowdhury, S., Ketcham, S. A., Schroer, T. A. & Lander, G. C. Structural organization of the dynein-dynactin complex bound to microtubules. *Nat. Struct. Mol. Biol.* **22**, 345–347 (2015).
9. Bharat, T. A. & Scheres, S. H. Resolving macromolecular structures from electron cryo-tomography data using subtomogram averaging in RELION. *Nat. Protoc.* **11**, 2054–2065 (2016).
10. Goddard, T. D., Huang, C. C. & Ferrin, T. E. Visualizing density maps with UCSF Chimera. *J. Struct. Biol.* **157**, 281–287 (2007).
11. Schmidt, H., Gleave, E. S. & Carter, A. P. Insights into dynein motor domain function from a 3.3-Å crystal structure. *Nat. Struct. Mol. Biol.* **19**, 492–497 (2012).
12. Bhabha, G. et al. Allosteric communication in the dynein motor domain. *Cell* **159**, 857–868 (2014).
13. Gutierrez, P. A., Ackermann, B. E., Vershinin, M. & McKenney, R. J. Differential effects of the dynein-regulatory factor Lissencephaly-1 on processive dynein-dynactin motility. *J. Biol. Chem.* **292**, 12245–12255 (2017).
14. Urnavicius, L. et al. Cryo-EM shows how dynactin recruits two dyneins for faster movement. Preprint at https://www.biorxiv.org/content/early/2017/08/31/183160 (2017).
15. Schroeder, C. M. & Vale, R. D. Assembly and activation of dynein-dynactin by the cargo adaptor protein Hook3. *J. Cell Biol.* **214**, 309–318 (2016).
16. Olenick, M. A., Tokito, M., Boczkowska, M., Dominguez, R. & Holzbaur, E. L. Hook adaptors induce unidirectional processive motility by enhancing the dynein-dynactin interaction. *J. Biol. Chem.* **291**, 18239–18251 (2016).
17. Rai, A. K., Rai, A., Ramaiya, A. J., Jha, R. & Mallik, R. Molecular adaptations allow dynein to generate large collective forces inside cells. *Cell* **152**, 172–182 (2013).
18. Rai, A. et al. Dynein clusters into lipid microdomains on phagosomes to drive rapid transport toward Lysosomes. *Cell* **164**, 722–734 (2016).
19. Wemmer, K. A. & Marshall, W. F. Flagellar motility: all pull together. *Curr. Biol.* **14**, R992–R993 (2004).
20. Ishikawa, T. Structural biology of cytoplasmic and axonemal dyneins. *J. Struct. Biol.* **179**, 229–234 (2012).
21. Lin, J., Okada, K., Raytchev, M., Smith, M. C. & Nicastro, D. Structural mechanism of the dynein power stroke. *Nat. Cell Biol.* **16**, 479–485 (2014).
22. Torisawa, T. et al. Autoinhibition and cooperative activation mechanisms of cytoplasmic dynein. *Nat. Cell Biol.* **16**, 1118–1124 (2014).
23. Xu, J., Shu, Z., King, S. J. & Gross, S. P. Tuning multiple motor travel via single motor velocity. *Traffic* **13**, 1198–1205 (2012).
24. Derr, N. D. et al. Tug-of-war in motor protein ensembles revealed with a programmable DNA origami scaffold. *Science* **338**, 662–665 (2012).
25. Kotani, N., Sakakibara, H., Burgess, S. A., Kojima, H. & Oiwa, K. Mechanical properties of inner-arm dynein-f (dynein I1) studied with in vitro motility assays. *Biophys. J.* **93**, 886–894 (2007).

Author contributions

D.A.G. and S.C. prepared the MT-bound complexes and performed all EM data collection. D.A.G., S.C., Y.X., and G.C.L. performed the image analyses. D.A.G., S.C., R.J.M., T.A.S., and G.C.L. contributed to the experimental design and assembly of the manuscript.

Competing interests

The authors declare no competing financial interests.

Methods

Purification of MT-bound complexes. The cargo adaptor proteins GFP-BICD2N (residues 25–400) and SNAPf–Hook3 (residues 1–552) were recombinantly expressed and purified as described previously[5,8]. MT-bound DDB complexes were prepared from mouse brain tissue as described previously[8]. Isolation of MT-bound DDH complexes was performed using the same MT–DDB protocol, with a minor modification to incorporate aspects of a protocol established by Amos et al.[26] to enrich DDH complex on MTs. We initially removed bulk tubulin from the lysate by adding 6 µM Taxol and 0.2 mM GTP, performing one round of MT polymerization and then pelleting and discarding the polymerized MTs and MAPs by centrifugation. In order to prevent endogenous dynein from associating with the MTs before pelleting, 0.5 mM Mg^{2+}-ATP was added to the lysate, resulting in the lysate having a higher dynein-to-tubulin ratio. The remaining tubulin in the lysate was then polymerized by adding 10 µM Taxol and 1 mM GTP, and 4 mM Mg^{2+}-AMP-PNP and 500 nM of Hook3 were added to promote engagement of the DDH complexes to the MTs.

MT-engaged dynein was prepared from mouse brain using similar procedures as described for the MT–DDH complex, but to prevent the association of endogenous dynactin with dynein, the lysate was not supplemented with recombinant cargo adaptor proteins. The protocol for this work was approved by the TSRI IACUC office under protocol 14-0013.

Grid preparation for cryo-electron microscopy analysis. All samples were prepared for cryo-EM imaging in a similar manner. The complex-bound MT pellets were diluted 20-fold with PMEE buffer supplemented with 1 mM GTP, 4 mM Mg^{2+}-AMP-PNP, and 20 µM Taxol at room temperature. 5 nm colloidal gold (Ted Pella) was pretreated with BSA to prevent aggregation, as described previously[27]. Immediately before freezing, samples were diluted 60–120-fold and mixed with the pretreated colloidal gold (optimal dilution for each sample was determined by screening the cryo-EM grids at a range of concentrations). 4-µl aliquots of sample were applied to freshly plasma-cleaned (75% argon/ 25% oxygen mixture) UltrAuFoil grids (Quantifoil) containing holes 1.2 µm in diameter spaced 1.3 µm apart. Plunge freezing was performed using a custom-built manual plunging device. The grid was manually blotted from the side opposite to which the sample was applied with a Whatman 1 filter paper for 5–7 s to remove excess sample. After blotting, we immediately vitrified the grid with remaining sample by plunge freezing it into liquid-ethane slurry. The entire procedure was carried out in a cold room maintained at 4 °C and >90% relative humidity.

Cryo-electron tomography data acquisition. Tilt series for DDB–MT and DDH–MT samples were collected using a Thermo Fisher Titan Krios electron microscope operating at 300 keV and equipped with a Gatan K2 Summit direct electron detector. Data acquisition was performed using the UCSF tomography package[28] implemented within the Leginon automated data acquisition software[29]. Tilt series were acquired using a sequential tilting scheme, starting at 0° and increasing to +59° at 1° increments, then returning to 0° and increasing to –59° at 1° increments. Each tilt series was collected with a nominal defocus value that was randomly set between 6–8 µm for the DDB–MT dataset and 2–5 µm for the DDH–MT dataset. Each tilt was acquired as movies in counting mode using a dose rate of 5.3 e$^-$/pixel/s, with a per-frame exposure time of 80 ms and a dose of 0.09 e$^-$/Å^2. The total cumulative dose for each tilt series was 114 e$^-$/Å^2 and was distributed throughout the tilts based on the cosine of the tilt angle to account for changing sample thickness with increasing tilt. 154 and 126 tilt series were collected for DDB–MT and DDH–MT samples, respectively, at a nominal magnification of 14,000×, giving a calibrated pixel size of 2.13 Å/pixel at the detector level.

Tilt series for the dynein–MT sample were collected on a Thermo Fisher Arctica electron microscope operating at 200 keV and equipped with a Gatan K2 Summit direct electron detector operating in movie mode, as described above. The total cumulative dose and dose distribution for each tilt series were the same as described for DDB–MT and DDH–MT datasets. Data were collected using the Leginon package[29] with an alternating tilt scheme[30]. A total of 58 tilt series were collected at a nominal magnification of 17,500×, giving a calibrated pixel size of 2.33 Å/pixel at the detector level.

Tomogram reconstruction. Image processing and tomogram reconstructions were performed in a similar fashion for all samples. Movie frames for each tilt were translationally aligned to account for beam-induced motion and drift using the GPU frame alignment program MotionCorr[31]. A frame offset of 7 and a B factor of 2,000 pixels were used for frame alignment. The raw tilts were initially Fourier-binned by a factor of 2. All micrographs were aligned using the 5-nm gold beads as fiducial markers and further binned by a factor of 2 (final pixel size of 8.52 Å/pixel for DDB–MT and DDH–MT datasets and 9.32 Å/pixel for the dynein–MT dataset) for reconstruction in the IMOD package[32]. Tomograms were reconstructed using simultaneous iterative reconstruction technique (SIRT) with seven iterations in IMOD, which provided sufficient contrast for the purposes of particle selection. Tomograms were also reconstructed by weighted back projection (WBP) for the purposes of subtomogram averaging.

Subtomogram averaging and data processing. Intact DDB–MT, DDH–MT, or dynein–MT complexes were completely embedded in vitreous ice, such that they fully encircled the MTs, providing all possible views of the complexes attached to MTs (top, side, and bottom 'views' of MT–bound dynein complexes). Subvolumes containing DDB–MT, DDH–MT, or dynein–MT were manually picked from SIRT-reconstructed tomograms with the EMAN2 single-particle tomography boxer program[33]. Complexes above or below the MTs when viewed along the z axis were readily identifiable when examining the z slices above or below the MT. Picked coordinates for each subvolume were imported into the RELION 1.4 subtomogram averaging workflow[9]. 502 and 303 subvolumes were extracted from the WBP reconstructions of the DDB–MT and DDH–MT datasets, respectively. Subvolumes were extracted using a cube size of 96 voxels for the DDB–MT dataset and 84 voxels for the DDH–MT dataset. Reference-free 3D classification in RELION did not yield any structures resembling dynein or dynactin complexes and instead predominantly produced averages of MTs. Attempts to remove signal from MTs by applying binary masks did not improve our ability to resolve the MT-bound complexes. To overcome this issue, we developed an assisted 3D subtomogram averaging procedure (Supplementary Fig. 3), wherein we manually docked the available reconstruction of the dynein tail–dynactin–BICD2N (TBD) complex (EMDB-2860 (ref. [7])) into the DDB–MT or DDH–MT subvolumes using UCSF Chimera[10]. The docked densities provided the rotational and translational parameters to generate initial subtomogram averages of the DDB and DDH complexes. These initial averages contained recognizable molecular features consistent with the previously published TDB structure (PDB 2AFU)[7] (Supplementary Fig. 3b). To better resolve different components (dynein tail–adaptor–dynactin region and dynein motors) of the DDB and DDH complexes, focused 3D refinements were performed using 3D ellipsoidal binary masks corresponding to the individual subregions, and the same particles were used for refinement of the individual subunit (i.e., no particles were excluded when refining individual components) (Supplementary Fig. 3c). For each component, 3D refinement was performed in RELION using the initial alignment parameters, with a HEALPix order of 3, an angular step size of 7.5°, and an offset range of 5 pixels. All particles were used in the focused 3D refinement to produce better-resolved reconstructions of the individual components of the MT-bound dynein complexes. These refinements resulted in better-defined subregions of the MT–DDB and MT–DDH complexes (Supplementary Fig. 3c). The final resolutions of these reconstructions are conservatively estimated to be ~38 Å (by Fourier shell correlation at a 0.5 cutoff) (Supplementary Figs. 5 and 7a).

Composite reconstructions of the DDB–MT and DDH–MT complexes were generated by aligning and stitching together the focused reconstructions using the "vop maximum" function in UCSF Chimera[10], which retains the maximum voxel values of overlapping volumes. The following crystal structures and atomic models of individual components were rigid-body docked into the final, combined DDB–MT structure using UCSF chimera[10]: dynein AMP-PNP-bound AAA+ ATPase motor domains (PDB 4W8F)[12], dynein motor-domain stalk (PDB 3VKG)[34], dynein MTBD in a high-affinity state (PDB 3J1T)[35], human cytoplasmic dynein-1 heavy chain and associated subunits (IC, LIC, LC7) bound to dynactin and N-terminal GFP-BICD2N (PDB 5NW4, PDB 5NVS)[2], and GFP (PDB 1GFL)[36].

Although the presence of an additional tail dimer and appearance of four dynein motors in the DDB subtomogram average serve as internal controls that preclude the introduction of model bias into our refinement procedure, we performed additional control experiments to rule out this possibility. We first tested the ability of our subvolumes to reproduce the well-resolved dynein tail–adaptor–dynactin region after focused refinement of the MDs. Focused refinement of the motors resulted in misalignment of the dynein tail–adaptor–dynactin region, resulting in poorly resolved dynactin density (Supplementary Fig. 4a). Re-refining this region using an ellipsoidal binary mask reproduced the dynactin with well-resolved structural features. Next, we docked the TDB complex (EMDB-2860, (ref. [7])) into the subvolumes using randomly assigned Euler angles and performed the same refinement strategy outlined above. This was repeated using three unique seeds for randomization, and in each case, the resulting subtomogram did not yield a recognizable complex (Supplementary Fig. 4b).

229 dynein–MT subvolumes were extracted from the WBP tomograms with a cube size of 96 voxels. As with the DDB and DDH datasets, ab initio 3D classification mostly resulted in MT averages and did not yield any recognizable dynein structures. We attempted to perform an assisted alignment approach, which involved placing spherical markers on the individual dynein MDs using IMOD[32]. However, because of the variability of the intermotor spacing and the disordered arrangement of the dyneins relative to the MTs, we were unable to produce a 3D subtomogram average of MT-bound dimeric dynein. The spherical markers in 3D tomograms were used to measure the 3D intermotor distances shown in Supplementary Fig. 8. Only motors that were visibly connected as a dimer were used for MD–MD distance measurements.

Life Sciences Reporting Summary. Further information on experimental design is available in the Life Sciences Reporting Summary.

Data availability. Reconstructed maps of DDB–MT and DDH–MT were deposited in EM Data Bank under accession codes EMD-7000 and EMD-7001, respectively. The datasets that support the findings of this study are also available from the corresponding author upon reasonable request.

References

26. Amos, L. A. Brain dynein crossbridges microtubules into bundles. *J. Cell Sci.* **93**, 19–28 (1989).
27. Iancu, C. V. et al. Electron cryotomography sample preparation using the Vitrobot. *Nat. Protoc.* **1**, 2813–2819 (2006).
28. Suloway, C. et al. Fully automated, sequential tilt-series acquisition with Leginon. *J. Struct. Biol.* **167**, 11–18 (2009).
29. Suloway, C. et al. Automated molecular microscopy: the new Leginon system. *J. Struct. Biol.* **151**, 41–60 (2005).
30. Hagen, W. J. H., Wan, W. & Briggs, J. A. G. Implementation of a cryo-electron tomography tilt-scheme optimized for high resolution subtomogram averaging. *J. Struct. Biol.* **197**, 191–198 (2017).
31. Li, X. et al. Electron counting and beam-induced motion correction enable near-atomic-resolution single-particle cryo-EM. *Nat. Methods* **10**, 584–590 (2013).
32. Kremer, J. R., Mastronarde, D. N. & McIntosh, J. R. Computer visualization of three-dimensional image data using IMOD. *J. Struct. Biol.* **116**, 71–76 (1996).
33. Galaz-Montoya, J. G., Flanagan, J., Schmid, M. F. & Ludtke, S. J. Single particle tomography in EMAN2. *J. Struct. Biol.* **190**, 279–290 (2015).
34. Kon, T. et al. The 2.8 Å crystal structure of the dynein motor domain. *Nature* **484**, 345–350 (2012).
35. Redwine, W. B. et al. Structural basis for microtubule binding and release by dynein. *Science* **337**, 1532–1536 (2012).
36. Yang, F., Moss, L. G. & Phillips, G. N. Jr. The molecular structure of green fluorescent protein. *Nat. Biotechnol.* **14**, 1246–1251 (1996).

nature research

Corresponding author(s): Gabriel C. Lander

☐ Initial submission ☐ Revised version ☒ Final submission

Life Sciences Reporting Summary

Nature Research wishes to improve the reproducibility of the work that we publish. This form is intended for publication with all accepted life science papers and provides structure for consistency and transparency in reporting. Every life science submission will use this form; some list items might not apply to an individual manuscript, but all fields must be completed for clarity.

For further information on the points included in this form, see Reporting Life Sciences Research. For further information on Nature Research policies, including our data availability policy, see Authors & Referees and the Editorial Policy Checklist.

▶ Experimental design

1. **Sample size**

   Describe how sample size was determined.

   > N/A

2. **Data exclusions**

   Describe any data exclusions.

   > N/A

3. **Replication**

   Describe whether the experimental findings were reliably reproduced.

   > N/A

4. **Randomization**

   Describe how samples/organisms/participants were allocated into experimental groups.

   > N/A

5. **Blinding**

   Describe whether the investigators were blinded to group allocation during data collection and/or analysis.

   > N/A

   Note: all studies involving animals and/or human research participants must disclose whether blinding and randomization were used.

6. **Statistical parameters**

   For all figures and tables that use statistical methods, confirm that the following items are present in relevant figure legends (or in the Methods section if additional space is needed).

n/a	Confirmed	
☐	☒	The exact sample size (*n*) for each experimental group/condition, given as a discrete number and unit of measurement (animals, litters, cultures, etc.)
☐	☒	A description of how samples were collected, noting whether measurements were taken from distinct samples or whether the same sample was measured repeatedly
☒	☐	A statement indicating how many times each experiment was replicated
☒	☐	The statistical test(s) used and whether they are one- or two-sided (note: only common tests should be described solely by name; more complex techniques should be described in the Methods section)
☒	☐	A description of any assumptions or corrections, such as an adjustment for multiple comparisons
☒	☐	The test results (e.g. *P* values) given as exact values whenever possible and with confidence intervals noted
☒	☐	A clear description of statistics including central tendency (e.g. median, mean) and variation (e.g. standard deviation, interquartile range)
☒	☐	Clearly defined error bars

   See the web collection on statistics for biologists for further resources and guidance.

▶ Software

Policy information about availability of computer code

7. Software

Describe the software used to analyze the data in this study.

> Leginon, MotionCor2, IMOD, EMAN2, RELION, Chimera

For manuscripts utilizing custom algorithms or software that are central to the paper but not yet described in the published literature, software must be made available to editors and reviewers upon request. We strongly encourage code deposition in a community repository (e.g. GitHub). *Nature Methods* guidance for providing algorithms and software for publication provides further information on this topic.

▶ Materials and reagents

Policy information about availability of materials

8. Materials availability

Indicate whether there are restrictions on availability of unique materials or if these materials are only available for distribution by a for-profit company.

> None

9. Antibodies

Describe the antibodies used and how they were validated for use in the system under study (i.e. assay and species).

> N/A

10. Eukaryotic cell lines

a. State the source of each eukaryotic cell line used.

> N/A

b. Describe the method of cell line authentication used.

> N/A

c. Report whether the cell lines were tested for mycoplasma contamination.

> N/A

d. If any of the cell lines used are listed in the database of commonly misidentified cell lines maintained by ICLAC, provide a scientific rationale for their use.

> N/A

▶ Animals and human research participants

Policy information about studies involving animals; when reporting animal research, follow the ARRIVE guidelines

11. Description of research animals

Provide details on animals and/or animal-derived materials used in the study.

> For each dataset, four Mouse C57BL/6J Male brains were harvested for protein purification of dynein/dynactin/microtubule complexes

Policy information about studies involving human research participants

12. Description of human research participants

Describe the covariate-relevant population characteristics of the human research participants.

> N/A